SUBMILLIMETER ARRAY IDENTIFICATION OF THE MILLIMETER-SELECTED GALAXY SSA22-AzTEC1: A PROTOQUASAR IN A PROTOCLUSTER?

Y. TAMURA[1,2], D. IONO[1], D. J. WILNER[3], M. KAJISAWA[4,5], Y. K. UCHIMOTO[6], D. M. ALEXANDER[7], A. CHUNG[3,8], H. EZAWA[9],
B. HATSUKADE[1,6], T. HAYASHINO[4], D. H. HUGHES[10], T. ICHIKAWA[4], S. IKARASHI[6], R. KAWABE[1,11], K. KOHNO[6,12],
B. D. LEHMER[7,13,14], Y. MATSUDA[7], K. NAKANISHI[9], T. TAKATA[9], G. W. WILSON[15], T. YAMADA[4], AND M. S. YUN[15]

[1] Nobeyama Radio Observatory, National Astronomical Observatory of Japan, Nobeyama, Minamimaki, Minamisaku, Nagano 384-1305, Japan;
yoichi.tamura@nao.ac.jp
[2] Department of Astronomy, The University of Tokyo, Hongo, Bunkyo-ku, Tokyo 113-0033, Japan
[3] Harvard-Smithsonian Center for Astrophysics, 60 Garden Street, Cambridge, MA 02138, USA
[4] Astronomical Institute, Tohoku University, Aramaki, Aoba, Sendai, Miyagi 980-8578, Japan
[5] Research Center for Space and Cosmic Evolution, Ehime University, Bunkyo-cho, Matsuyama, Ehime 790-8577, Japan
[6] Institute of Astronomy, The University of Tokyo, Osawa, Mitaka, Tokyo 181-0015, Japan
[7] Department of Physics, Durham University, Durham DH1 3LE, UK
[8] Department of Astronomy, Yonsei University, Seoul 120-749, Korea
[9] National Astronomical Observatory of Japan, Osawa, Mitaka, Tokyo 181-8588, Japan
[10] Instituto Nacional de Astrofísica, Optica y Electronica, Aptdo. Postal 51 y 216, 72000 Puebla, Mexico
[11] Department of Astronomy, School of Science, Graduate University for Advanced Studies, Osawa, Mitaka, Tokyo 181-8588, Japan
[12] Research Center for the Early Universe, School of Science, The University of Tokyo, Hongo, Bunkyo, Tokyo 113-0033, Japan
[13] The Johns Hopkins University, Department of Physics and Astronomy, Baltimore, MD 21218, USA
[14] NASA Goddard Space Flight Center, Code 662, Greenbelt, MD 20771, USA
[15] Department of Astronomy, University of Massachusetts, 710 North Pleasant Street, Amherst, MA 01003, USA

ABSTRACT

We present results from Submillimeter Array (SMA) $860\,\mu$m subarcsecond astrometry and multiwavelength observations of the brightest millimeter ($S_{1.1\mathrm{mm}} = 8.4$ mJy) source, SSA22-AzTEC1, found near the core of the SSA22 protocluster that is traced by Lyα-emitting galaxies at $z = 3.09$. We identify a $860\,\mu$m counterpart with a flux density of $S_{860\,\mu\mathrm{m}} = 12.2 \pm 2.3$ mJy and absolute positional accuracy that is better than 0″.3. At the SMA position, we find radio-to-mid-infrared counterparts, whilst no object is found in Subaru optical and near-infrared deep images at wavelengths $\leqslant 1\,\mu$m ($J > 25.4$ in AB, 2σ). The photometric redshift estimate, using flux densities at $\geqslant 24\,\mu$m, indicates $z_{\mathrm{phot}} = 3.19^{+0.26}_{-0.35}$, consistent with the protocluster redshift. We then model the near-to-mid-infrared spectral energy distribution (SED) of SSA22-AzTEC1, and find that the SED modeling requires a large extinction ($A_V \approx 3.4$ mag) of starlight from a stellar component with $M_{\mathrm{star}} \sim 10^{10.9}\,M_{\odot}$, assuming $z = 3.1$. Additionally, we find a significant X-ray counterpart with a very hard spectrum ($\Gamma_{\mathrm{eff}} = -0.34^{+0.57}_{-0.61}$), strongly suggesting that SSA22-AzTEC1 harbors a luminous active galactic nuclei (AGNs; $L_X \approx 3 \times 10^{44}$ erg s^{-1}) behind a large hydrogen column ($N_{\mathrm{H}} \sim 10^{24}$ cm^{-2}). The AGN, however, is responsible for only ∼10% of the bolometric luminosity of the host galaxy, and therefore the star formation activity likely dominates the submillimeter emission. It is possible that SSA22-AzTEC1 is the first example of a protoquasar growing at the bottom of the gravitational potential underlying the SSA22 protocluster.

Key words: galaxies: formation – galaxies: starburst – infrared: galaxies – quasars: general – submillimeter: galaxies – X-rays: galaxies

Online-only material: color figures

1. INTRODUCTION

Mounting evidence suggests that submillimeter-selected galaxies (SMGs; Smail et al. 1997; Hughes et al. 1998; Barger et al. 1998; Blain et al. 2002; Scott et al. 2008, 2010; Perera et al. 2008; Austermann et al. 2009, 2010) are the most massive, gas-rich systems at $z \sim 2$–3 with far-infrared (FIR) luminosity of $L_{\mathrm{FIR}} \sim 10^{12}$–$10^{13}\,L_{\odot}$ (e.g., Borys et al. 2005; Greve et al. 2005; Solomon & Vanden Bout 2005; Tacconi et al. 2006; Dye et al. 2008). Their extreme luminosity is likely produced by intense episodes of star formation, and therefore it is likely that SMGs are undergoing rapid growths of their stellar components. A main catalyst for starburst is believed to be major mergers of gas-rich galaxies (e.g., Smail et al. 1998). The merger event is probably an efficient mechanism to transfer cold gas into the nuclear region and fuel the star formation and nuclear activity, as suggested by hydrodynamical simulations (e.g., Hopkins et al. 2006; Narayanan et al. 2010).

An outstanding issue surrounding the SMG population is that dusty starburst galaxies at high redshift can relate to early growth of supermassive black holes seen at the present day. It is believed that radiation pressure from accretion disks around supermassive black holes efficiently strips away the obscuring gas and dust that fuel star formation activities in their host galaxies, making accreting massive black holes an important regulator of galaxy formation and evolution (e.g., Silk & Rees 1998; Fabian 1999; Di Matteo et al. 2005). Early (sub)millimeter surveys have revealed that host galaxies of powerful active galactic nuclei (AGNs) at high z are often submillimeter bright (e.g., McMahon et al. 1994; Dunlop et al. 1994; Isaak et al. 1994; Ivison 1995; Archibald et al. 2001; Stevens et al. 2003, 2010; Reuland et al. 2004). Multiwavelength diagnostics indicate that a substantial fraction (20%–50%) of SMGs have AGNs at their center, suggesting a causal connection between the SMG phenomena (i.e., bulge formation) and massive black hole growth (Alexander et al. 2003, 2005a; Borys et al. 2004;

Swinbank et al. 2004; Takata et al. 2006; Menéndez-Delmestre et al. 2009; Hainline et al. 2009). SMGs have a volume number density and a redshift distribution similar to those of quasars (e.g., Chapman et al. 2005), allowing many to propose a hypothesis that the populations of SMGs and quasars can be evolutionarily linked. Moreover, black hole masses for SMGs appear to be systematically smaller than those found in quasars (Alexander et al. 2008), implying that some fraction of SMGs with obscured X-ray sources are at a *protoquasar* phase, where the black hole is growing more rapidly than in typical galaxies and is about to blow off the thick surrounding gas clouds by accretion-related outflows from the black hole (e.g., Sanders et al. 1988; Kawakatu et al. 2003, 2006, 2007; Granato et al. 2004, 2006; Alexander et al. 2005b; Borys et al. 2005; Kawakatu & Wada 2009).

Theoretical studies of cosmic structure formation in a cold dark matter (CDM) universe (e.g., Kauffmann 1996) predict accelerated and correlated growths of galaxies and black holes in high-density environments, such as protoclusters of galaxies, which are embedded within the most massive dark matter halos collapsing in the early universe. It is natural to expect that the merger rate should be enhanced in high-density regions of galaxies, and in fact, number excesses of SMGs have been tentatively claimed toward known overdensities around high-redshift radio galaxies (Ivison et al. 2000; Stevens et al. 2003). Hence, the idea naturally arises that SMGs that host accreting massive black holes tightly relate to high-z large-scale structures.

The $z = 3.09$ SSA22 protocluster was originally identified as a significant concentration, in redshift space, of Lyman break galaxies (Steidel et al. 1998). The surface density of those Lyman break galaxies is ∼6 times higher than in the field, making this concentration one of the highest density regions known to date. Theoretical modeling indicates that the protocluster will evolve into a rich cluster with a total mass of $\gtrsim 10^{15} M_\odot$ at the present day (Steidel et al. 1998). The protocluster has also been found to contain a factor of ∼3–6 overdensity of Lyα emitters (Steidel et al. 2000; Hayashino et al. 2004). Subsequent spectroscopic follow-up of these Lyα emitters, which are believed to be star-forming building blocks of galaxies, has revealed a large-scale filamentary structure extending across ∼60 h^{-1} Mpc or more (Matsuda et al. 2005). In this structure, many extended Lyα-emitting objects (Lyα blobs, Steidel et al. 2000; Hayashino et al. 2004; Matsuda et al. 2004) have been found, which are thought to be a formation site of massive galaxies (e.g., Geach et al. 2005, 2007). Uchimoto et al. (2008) have suggested a density enhancement of another massive population of distant red galaxies (DRGs; Franx et al. 2003; van Dokkum et al. 2003). Furthermore, Lehmer et al. (2009a) has found a remarkable enhancement in AGNs in SSA22 compared to $z \approx 3$ field galaxies. Thus, the SSA22 protocluster is an ideal site for studying the co-evolution of massive galaxies and powerful AGNs in a high-density environment.

Recently, a large-area 1.1 mm survey toward SSA22 has been performed (Tamura et al. 2009) using the AzTEC 1.1 mm camera (Wilson et al. 2008a) mounted on the ASTE 10 m telescope (Ezawa et al. 2004). They have mapped a ≈390 arcmin² region of the protocluster and revealed 30 SMGs. Among them, the brightest 1.1 mm source SSA22-AzTEC1 ($S_{1.1mm} = 8.4^{+0.8}_{-1.0}$ mJy) was found near the core of the protocluster, which hints that it could evolve into a massive elliptical in this descendant of the protocluster.

However, the multiwavelength counterparts to SSA22-AzTEC1 cannot be easily identified because of the coarse beam (30″ in an FWHM) of the AzTEC/ASTE instrument and multiple candidates within the error circle. For SMG astrometry, centimeter radio interferometers have often been employed so far, but they are not sensitive to SMGs at $z > 3$, since radio flux rapidly dims with increasing redshift. In contrast, imaging of the dust emission in submillimeter waveband benefits from the strong negative K-correction, and its flux density is almost constant for a galaxy with a fixed FIR luminosity at redshifts $z \approx$ 1–10 (Blain & Longair 1993). Recent high spatial resolution observations (e.g., Iono et al. 2006a; Younger et al. 2007, 2009; Wang et al. 2007, 2009) using the Submillimeter Array (SMA; Ho et al. 2004) have uncovered a substantial population of high-z SMGs that are undetected in the radio and optical, suggesting that we would miss some high-z SMGs by the radio selection method. Another potential hazard of using wavelengths other than (sub)millimeter is that a simple extraction of the nearest radio or mid-infrared (MIR) source within an error circle could lead to misidentification of counterparts to SMGs (e.g., Cowie et al. 2009), though it is difficult to estimate an accurate percentage of misidentifications.

In this paper, we present the results from SMA 860 μm observations and multiwavelength properties of the brightest 1.1 mm source SSA22-AzTEC1 found in the SSA22 protocluster field. We use spectral energy distributions (SEDs) to constrain its photometric redshift. We also model an SED in the near-infrared (NIR) to MIR to estimate the physical properties of the stellar component. We then utilize X-ray data to identify AGN activity. The multiwavelength study of the 1.1 mm source provides a fairly unique opportunity to investigate the growth of cosmic hierarchical structures over quite different spatial scales from AGNs (∼1 pc) to large-scale structures (∼10 Mpc): co-evolution of supermassive black hole and its host galaxy, and preferential growth of a massive galaxy with a powerful AGN in a high-density environment in the early universe, which is one of the main concerns in recent astrophysics.

Throughout this paper, we will assume an $\Omega_M = 0.3$, $\Omega_\Lambda = 0.7$ cosmology with $H_0 = 70$ km s^{-1} Mpc^{-1} as cosmological parameters. An angular scale of 1″ corresponds to 7.6 kpc physical size at $z = 3.1$.

2. DATA AND OBSERVATIONS

2.1. SMA Observations and Data Reduction

The SMA is an interferometer operating at submillimeter wavebands (230, 350, and 690 GHz) that consists of eight 6 m antennas located at Mauna Kea, Hawaii. We used the "compact (C)" configuration of the SMA. Seven of the eight antennas were operational in the observing track, which gave a range of projected baseline lengths of 6–60 m, which corresponds to 7–90 kλ (i.e., projected antenna separation lengths measured in units of an observing wavelength λ, which determine the resultant spatial resolution of interferometric images). The heterodyne receivers equipped with a superconductor–insulator–superconductor (SIS) mixer were tuned to 355.843 GHz (upper sideband, hereafter USB) and 345.843 GHz (lower sideband, hereafter LSB) for observing the continuum emission. We obtained 2 GHz total bandwidth in each sideband. The FWHM of the primary beam[16] at the

---

[16] The primary beam is a point response function (PRF) of a single-dish element of interferometers, and provides a field of view of an interferometric synthesized image.

frequency is $34''$, which is comparable to the AzTEC/ASTE spatial resolution and enough to cover the 2σ error circle of the AzTEC/ASTE positional uncertainty ($\lesssim 20''$).

The data were obtained on 2008 September 6. The conditions were "excellent" (zenith opacities at 225 GHz, $\tau_{225\,\mathrm{GHz}} = 0.04$–$0.06$, and the typical rms phase fluctuation at 350 GHz, $\Delta\phi \simeq 10°$), and the double sideband system noise temperatures throughout the track were 150–300 K. The phase tracking center for the target source SSA22-AzTEC1 was set to R.A. (J2000) = $22^\mathrm{h}17^\mathrm{m}32\overset{s}{.}4$, decl. (J2000) = $+0°17'35''\!.47$, which is the centroid derived from AzTEC observations of SSA22-AzTEC1. Each visibility was integrated for 30 s, which is short enough to avoid decorrelation caused by atmospheric phase fluctuations. The total integration time on SSA22-AzTEC1 was 8.8 ks or 2.5 hr. The target source benefits from having a very good nearby gain calibrator, a 2 Jy radio-loud quasar 3C446 ($5\overset{\circ}{.}6$ away from the target). 3C446 was observed every 20 minutes to calibrate the gain variation. 3C454.3 and Uranus were observed at the end of the track for bandpass and flux calibration, respectively. The total integration time on 3C454.3 was 60 minutes.

A baseline error of $\sim 0.1\lambda$ will yield a systematic positional error of an order $0''\!.02$, which is much below the statistical error ($0''\!.13$; see Section 3). To further check our astrometry, a fainter, nearer radio-loud quasar J2218–035 (R.A. (J2000) = $22^\mathrm{h}18^\mathrm{m}52\overset{s}{.}0377$, decl. (J2000) = $-3°35'36''\!.879$, which is $3\overset{\circ}{.}8$ away from SSA22) with a precise known position was observed for verification of the accurate transfer of the phase solutions and checking the astrometric precision.

The visibility data were calibrated using the IDL-based SMA standard reduction package, MIR. We did not need to flag out any of the data because of the excellent observing conditions. The flux density of a gain calibrator 3C446 at $860\,\mu$m was estimated to be 2.12 ± 0.11 Jy. The calibrated visibility data in USB and LSB were compiled and imaged (Fourier transformed) using the MIRIAD (Sault et al. 1995) task, `invert`. The resultant size of the natural-weighted synthesized beam is $3''\!.43 \times 1''\!.92$ (position angle P.A. = $34\overset{\circ}{.}3$). Since the spatial frequency coverage is fairly poor because of short observing time and the declination very close to zero, the resultant map suffers from high side-lobe level of 60%. We extensively CLEAN-ed the dirty image blindly (i.e., without constraining the region of interest to model the intensity field), restored the clean model, and convolved it with the clean beam (a two-dimensional Gaussian with $3''\!.43 \times 1''\!.92$, P.A. = $34\overset{\circ}{.}3$). The uncertainty of absolute flux scaling is estimated to be better than 15%.

2.2. Multiwavelength Data

We have multiwavelength data from the radio to the X-ray, which were already taken and cover the position of SSA22-AzTEC1. Here, we provide a brief summary of the existing data and, in part, newly taken data.

We use 1.4 GHz (20 cm) radio data obtained toward SSA22 that were already published in Chapman et al. (2003). The SSA22 field was observed in the B configuration of the Very Large Array (VLA), yielding a $\simeq 5''$ synthesized beam. The on-source time $t_{\mathrm{integ}} = 12$ hr resulted in an rms noise level over the AzTEC coverage to be $\simeq 12\,\mu$Jy beam^{-1}.

We retrieve MIR photometry data from the *Spitzer* archive to search for a counterpart at MIR wavelengths and measure the flux densities. We use 3.6, 4.5, 5.8, and $8.0\,\mu$m images obtained with the Infrared Array Camera (IRAC; Fazio et al. 2004), and 24 and $160\,\mu$m images obtained with the Multi-band Imaging Photometer for *Spitzer* (MIPS; Rieke et al. 2004). There

is no $70\,\mu$m data at the position of SSA22-AzTEC1. The basic calibrated data (BCD) of IRAC and MIPS are processed through masking, flat fielding, background matching, and mosaicking using the MOPEX (Mosaicking and Point Source Extraction) software, which is a package developed at the *Spitzer* Science Center for astronomical image processing, along with calibrated data retrieved from the *Spitzer* archive. Then point sources at 3.6, 4.5, 5.8, 8.0, and $24\,\mu$m are extracted using a MOPEX pipeline, APEX, by fitting the PRF for each band to each source candidate.

The deep NIR imaging observations of the SSA22 region have been performed by Uchimoto et al. (2008) using MOIRCS[17] (Ichikawa et al. 2006; Suzuki et al. 2008) mounted on the Subaru Telescope, Mauna Kea, Hawaii. A part of the NIR data are published elsewhere (Uchimoto et al. 2008), but we append NIR data that are newly taken with MOIRCS/Subaru (Y. K. Uchimoto et al. 2010, in preparation). Here, we describe a brief summary of the MOIRCS observations. The total exposure times of the J-, H-, and K_S-band imaging toward SSA22-AzTEC1 were 5820, 2765, and 4541 s, respectively. The stellar image sizes of the J, H, and K_S images are $0''\!.4$–$0''\!.5$, and the limiting magnitudes of the images are $J = 25.42$, $H = 24.99$, and $K_S = 25.08$ mag (2σ) in the AB system in a $1''$ diameter aperture.

In the photometry, IRAC and MOIRCS flux densities were measured as follows. In order to achieve higher signal-to-noise ratio (S/N), we first smoothed the IRAC and MOIRCS images so that their PRFs match that of the $8.0\,\mu$m image. Then we measured the flux densities of the NIR–MIR counterparts using a relatively small ($3''\!.0$ in diameter) aperture to avoid source confusion. The aperture corrections were performed for all of the NIR–MIR data by multiplying a scaling factor. We estimated this scaling factor by comparing the $3''$ aperture flux and a total flux, both of which were obtained for the $8.0\,\mu$m image since the $8.0\,\mu$m image was less susceptible to confusion noise than the other (smoothed) images (see Figure 3). The $8.0\,\mu$m total flux was measured with SExtractor `MAG_AUTO` (Bertin & Arnouts 1996).

Deep optical images in B, V, R, i', z', and NB497 bands taken with Suprime-Cam (Miyazaki et al. 2002) on Subaru are available at the position of SSA22-AzTEC1. NB497 is a narrow band filter centered at 497.7 nm, which is designed to search for strong Lyα emission in galaxies at $z = 3.06$–3.12. The details of the observations are described in Hayashino et al. (2004) and Matsuda et al. (2004, 2005). The average profile of a point source in the final images has an FWHM of $1''\!.0$. All of the optical photometry are measured with a $2''\!.0$ diameter aperture, and are corrected for the Galactic reddening of $E(B-V) = 0.062$. The limiting magnitudes after the correction are 28.2, 27.9, 28.3, 28.4, 28.1, and 27.4 (AB, 1σ) in B, NB497, V, R, i', and z' bands, respectively.

Recently, Lehmer et al. (2009a, 2009b) and Geach et al. (2009) have reported the ultra-deep (400 ks) *Chandra*/ACIS-I observations toward SSA22 (*Chandra* Deep Protocluster Survey). The survey covers a solid angle of ≈ 330 arcmin^2, and revealed 297 X-ray sources, which are listed in the "Main Source Catalog." The typical sensitivity limits were approximately 4.8×10^{-17} and 2.7×10^{-16} erg cm^{-2} s^{-1} for the 0.5–2 keV and 2–8 keV bands, respectively. These limits correspond to rest-frame 2–8 keV and 8–32 keV luminosities of 3.7×10^{42} and 2.1×10^{43} erg s^{-1}, respectively.

---

[17] Multi-Object InfraRed Camera and Spectrograph developed for the 8.2 m Subaru Telescope. See also a Web page at http://www.naoj.org/Observing/Instruments/MOIRCS/ for more details.
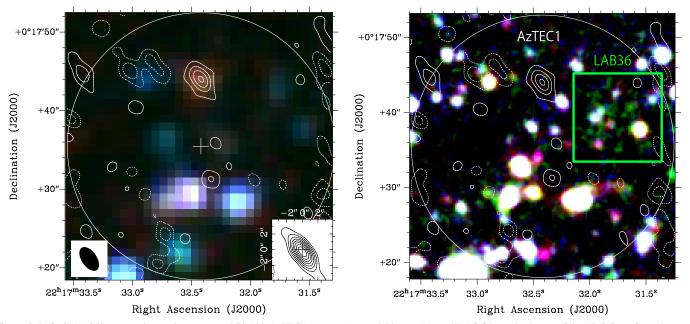
Figure 1. Left: SMA 860 μm continuum image toward SSA22-AzTEC1 (contours), overlaid on a *Spitzer*/IRAC false color image (8.0, 4.5, 3.6 μm for red, green, and blue, respectively). The SMA image is natural weighted and CLEANed. The circle shows a field of view of the SMA (an FWHM of the primary beam, which is the PRF of the SMA's single-dish elements) with a diameter of 34″. The synthesized beam is indicated as an ellipse on the bottom-left corner. Significant emission 8″ northward from the phase tracking center (cross) is evident. The peak intensity is 11.8 mJy beam^{-1}. The contours are drawn at $(-4, -2, 2, 4, 6, 8) \times \sigma$, where $1\sigma = 1.4$ mJy beam^{-1}. The negative levels are shown as dotted contours. In the inset of the left panel, we show the SMA 860 μm continuum image toward a test source J2218−035. The systematic offset of the nominal peak position from the phase tracking center (cross) is $(\Delta\text{R.A.}, \Delta\text{decl.}) = (0''.00 \pm 0''.13, -0''.31 \pm 0''.13)$. Right: SMA 860 μm continuum image toward SSA22-AzTEC1, overlaid on a Subaru/Suprime-Cam composite color image (blue, green, and red for B, NB497, and V bands, respectively). The green square denotes the position of the "mini" Lyα blob LAB36, which is located $\simeq 10''$ away from SSA22-AzTEC1. The circle shows a field of view of the SMA (34″ in diameter). The contours are drawn as described above.

3. RESULTS AND ANALYSES

3.1. SMA Results

In Figure 1, we found a clear (8.4σ) emission feature (AzTEC J221732.42+001744.0; we hereafter call the SMA source SSA22-AzTEC1 for convenience) located $\simeq 8''$ northward of the phase tracking center, strongly suggesting that this is the true counterpart to SSA22-AzTEC1. The resultant rms noise level is 1.4 mJy beam^{-1}, which is derived from a region away from the 860 μm counterpart. The peak intensity at 860 μm is 11.8 mJy beam^{-1}. The position is R.A. (J2000) = 22^{h}17^{m}32^s.42, decl. (J2000) = +0°17′44″.01. The inset panel of Figure 1 (lower-right) shows the 860 μm continuum image obtained toward the test source J2218−035, a strong radio quasar with an accurately known position, which was clearly detected with $\simeq 10\sigma$. The offset of the nominal peak position from the phase tracking center is $(\Delta\text{R.A.}, \Delta\text{decl.}) = (0''.00, -0''.31)$. The statistical positional error is estimated to be $0''.13$ following the formula $\Delta\theta_{\text{stat}} \simeq \sqrt{\theta_{\text{maj}}\theta_{\text{min}}}/2\text{S/N}$, where θ_{maj} and θ_{min} are the FWHM along the major and minor axis of the synthesized beam, respectively, and S/N is the signal-to-noise ratio of the source in the cleaned map. These suggest that the phase transfer is applied correctly and the absolute positional uncertainty through this SMA observation is estimated to be $<0''.33$.

We then investigate the flux density and the spatial extent of the source more accurately in the uv-domain. Figure 2 shows the visibility amplitudes versus projected baseline length for SSA22-AzTEC1, along with those expected for axisymmetric two-dimensional Gaussians with FWHM = $0''.5$, $1''.0$, and $2''.0$. The amplitudes are well described by a constant value ($S_{860\,\mu m} = 12.2 \pm 2.7$ mJy) as a function of projected baseline, suggesting that the source is not spatially resolved with the

SMA $2''$ beam and the upper limit on the source size is $\lesssim 1''$. The flux densities estimated from the map and the visibilities are slightly different (and still consistent) even though the source is not spatially resolved. The main difference is that the image is synthesized from the vector sum of all measurements of the visibilities while the total flux estimate in the spatial frequency domain is a scalar estimate of the vector-averaged subsets of the visibility data, which is prone to noise boosting by the fact that the visibility amplitude is always a positive quantity (e.g., Thompson et al. 2001).

Considering the flux density at 1.1 mm is $S_{1.1mm} = 8.4^{+0.8}_{-1.0}$ mJy, which is corrected for flux boosting, the 860–1100 μm flux density ratio is estimated to be $S_{860\,\mu m}/S_{1.1mm} = 1.45^{+0.47}_{-0.45}$. We scale our result to compare the flux ratio for 890 μm SMA follow-up of AzTEC sources, and find $S_{890\,\mu m}/S_{1.1mm} = 1.4 \pm 0.4$ for SSA22-AzTEC1. This value is consistent with 1.6 ± 0.7 for the SMA-identified AzTEC sources reported by Younger et al. (2007, 2009).

3.2. Possibility of Gravitational Lensing

The intrinsic flux density of SSA22-AzTEC1 may be lower if there is an amplification by gravitational lensing. While recent theoretical works (e.g., Paciga et al. 2009) imply that the fraction of ≈ 10 mJy submillimeter sources magnified by a factor of >2 is relatively small ($\sim 5\%$), there are many SMGs that are either known or strongly suspected to be lensed (e.g., Ivison et al. 1998; Downes & Solomon 2003; Dunlop et al. 2004; Kneib et al. 2004; Motohara et al. 2005; Wilson et al. 2008b; Knudsen et al. 2010; Swinbank et al. 2010). The small spatial size of SSA22-AzTEC1 measured with SMA (Figure 2) suggests that the high brightness of SSA22-AzTEC1 is unlikely due to a strong gravitational lensing effect caused by a foreground massive galaxy that would
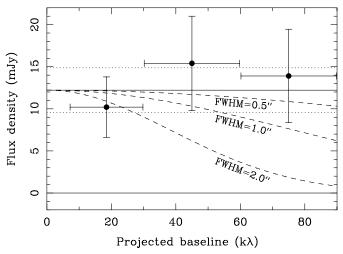
Figure 2. Visibility amplitudes vs. projected baseline length for SSA22-AzTEC1 (solid circles). There is no evidence that SSA22-AzTEC1 is spatially resolved with the SMA beam. The visibility amplitudes are well fitted to a constant value 12.2 ± 2.7 mJy (solid line) as a function of a projected baseline length. The 1σ confidence interval is shown as a region sandwiched between two dotted lines. The phase center is shifted to the peak position of the $860\,\mu$m counterpart to SSA22-AzTEC1. We also show visibility amplitudes expected for axisymmetric two-dimensional Gaussians with FWHM of $0\farcs5$, $1\farcs0$, and $2\farcs0$.

Table 1
Multiwavelength Counterparts to SSA22-AzTEC1

Instrument	Band	Flux Density	Unit	Reference
VLA	20 cm	42 ± 12	μJy	1
AzTEC/ASTE	$1100\,\mu$m	$8.2^{+0.8}_{-1.0}$ [a]	mJy	2
SMA	$860\,\mu$m	12.2 ± 2.7 [b]	mJy	1
MIPS/*Spitzer*	$24\,\mu$m	142 ± 18	μJy	1
IRAC/*Spitzer*	$8.0\,\mu$m	32.59 ± 2.27	μJy	1
	$5.8\,\mu$m	22.24 ± 1.87 [c]	μJy	1
	$4.5\,\mu$m	14.46 ± 0.76 [c]	μJy	1
	$3.6\,\mu$m	7.80 ± 0.50 [c]	μJy	1
MOIRCS/Subaru	$2.14\,\mu$m (K_S)	2.71 ± 0.63 [c]	μJy	1
	$1.64\,\mu$m (H)	2.13 ± 0.71 [c]	μJy	1
	$1.26\,\mu$m (J)	<1.12 [c]	μJy	1
S-Cam/Subaru	905 nm (z')	<0.080 [d]	μJy	1
	771 nm (i')	<0.042 [d]	μJy	1
	655 nm (R)	<0.032 [d]	μJy	1
	549 nm (V)	<0.035 [d]	μJy	1
	498 nm ($NB497$)	<0.050 [d]	μJy	1
	448 nm (B)	<0.038 [d]	μJy	1
ACIS-I/*Chandra*	0.5–8 keV	2.71 [e]	10^{-15} erg cm^{-2} s^{-1}	3
	0.5–2 keV	9.27 [e]	10^{-17} erg cm^{-2} s^{-1}	3
	2–8 keV	2.66 [e]	10^{-15} erg cm^{-2} s^{-1}	3

Notes.
[a] De-boosted flux density, i.e., flux density corrected for the flux bias due to confusion noise, with the 68% confidence interval.
[b] $860\,\mu$m flux density estimated from the visibility fitting.
[c] Aperture-corrected flux density measured using a $3\farcs0$ aperture after the image is smoothed so that the PSF matches that of $8.0\,\mu$m image.
[d] 2σ upper limit measured using a $2\farcs0$ aperture.
[e] Flux integrated over the ACIS-I bands.
References. (1) This work; (2) Tamura et al. 2009; (3) Lehmer et al. 2009b.

happen to be aligned in the direct line of sight. Moreover, if not in the direct line of sight, a lensing object must be found at an angular separation comparable to the Einstein radius. If a source at $z \gtrsim 1$ is located close to a foreground lensing object at $z \sim 0.3$, which is the favored geometry for efficiently lensing the background source, Einstein radii are $\sim 1''$–$2''$ and $\sim 30''$–$40''$ when the lensing object is a galaxy (dark halo mass of $10^{12}\,M_\odot$) and a cluster ($10^{15}\,M_\odot$), respectively. But, we do not see such a low-z massive galaxy $\sim 1''$–$2''$ away from SSA22-AzTEC1 although it would be easily detected in the Subaru K_S image. In SSA22, we find neither X-ray clusters, which are often found at $z \sim 0.3$, nor higher-z ($z \sim 1$) Sunyaev–Zel'dovich clusters, which should be observed in the AzTEC 1.1 mm map if they exist. It is also unlikely that the SSA22 protocluster at $z = 3.1$ itself is a lensing object because the SSA22 protocluster is by definition far from being virialized and should not have a deep potential well similar to those of low-z clusters. It is therefore likely that SSA22-AzTEC1 is not strongly magnified by gravitational lensing.

3.3. Multiwavelength Counterparts

At the position of the $860\,\mu$m source, we find a significant counterpart in the radio to MIR as well as in the X-ray, but the $860\,\mu$m source has no counterpart in the deep Subaru optical images. The flux densities and upper limits at radio to optical wavelengths are given in Table 1. The postage stamp images

at radio (20 cm) to near-ultraviolet (230 nm) wavelengths are presented in Figure 3.

Although there are multiple counterpart candidates in the radio map, we identify a radio counterpart ($S_{1.4\,\mathrm{GHz}} = 42 \pm 12\,\mu$Jy) at the position of the $860\,\mu$m source. The spectral index between $860\,\mu$m (350 GHz) and 20 cm (1.4 GHz) is $\alpha_{1.4}^{350} = 1.03 \pm 0.15$, suggesting a redshift of $z \sim 3$–4 on the basis of the redshift estimator proposed by Carilli & Yun (1999, 2000).

We find counterparts to the SMA position in all IRAC bands and MIPS $24\,\mu$m. However, we see no significant counterpart at $160\,\mu$m mainly due to heavy blending from infrared sources, which are located $\sim 15''$ southward from the $860\,\mu$m position (see Figure 3). These infrared sources have radio counterparts, and are the brightest at $24\,\mu$m in the SMA field of view. SSA22-AzTEC1 has red color in the *Spitzer*/IRAC bands, which is consistent with a $z \sim 3$ SMG. Figure 4 shows the color–color (IRAC 5.8–3.6 and 8.0–4.5 μm flux ratios) diagram for this source, SMGs with millimeter carbon monoxide (CO) or MIR *Spitzer*/IRS spectroscopy, and infrared-luminous
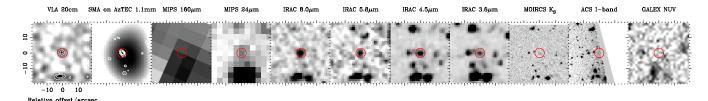

Figure 3. Postage stamp images of SSA22-AzTEC1 at radio to near-ultraviolet wavelengths. The red circles mark the SMA position.
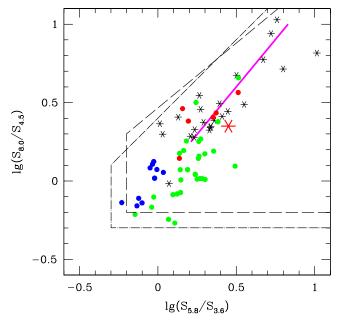(A color version of this figure is available in the online journal.)

Figure 4. *Spitzer*/IRAC $S_{5.8}/S_{3.6}$–$S_{8.0}/S_{4.5}$ color–color diagram for SMGs. The filled circles in blue, green, and red are SMGs with millimeter CO or *Spitzer*/IRS MIR spectroscopy at $z < 1.5$, $1.5 < z < 3.0$, and $z > 3.0$, respectively. The big red star is SSA22-AzTEC1, and indeed it is found near the transition region between $z < 3$ and $z > 3$ SMGs. The smaller, black stars represent infrared-luminous quasars from the FLS survey (Lacy et al. 2004), and it seems the $z > 3$ SMGs indeed have colors that overlap with the infrared power-law AGNs (thick magenta line). The color region on the plot that Yun et al. (2008) proposed for the identification of SMG counterparts is outlined by the dash-dotted line. The region for infrared-luminous AGNs proposed by Lacy et al. (2004) is outlined by the long-dashed line.

(A color version of this figure is available in the online journal.)

quasars from the *Spitzer* First Look Survey (FLS; Lacy et al. 2004). The 5.8–3.6 and 8.0–4.5 μm flux ratios of this object are $\log (S_{5.8}/S_{3.6}) = 0.46^{+0.03}_{-0.04}$ and $\log (S_{8.0}/S_{4.5}) = 0.35^{+0.02}_{-0.03}$, respectively. Indeed, it is found near the transition region between $z < 3$ and $z > 3$ SMGs with secure redshifts. It is seen in Figure 4 that infrared-luminous quasars identified in the FLS survey also have red IRAC colors, and it seems that the $z > 3$ SMGs indeed have colors that overlap with the infrared-luminous AGNs with a power-law spectrum in MIR (thick magenta line). We note that SSA22-AzTEC1 has the IRAC colors consistent with a $z \sim 3$ SMG, but all $z > 3$ SMGs also have IRAC colors very similar to the infrared power-law AGNs.

The SED of SSA22-AzTEC1 is well constrained at wavelengths $\gtrsim 3$ μm, but drops out at a wavelength of 1 μm ($J > 24.6$ in AB, 2σ) or shorter. We tentatively detect counterparts to SSA22-AzTEC1 in the H (3σ) and K_S bands (4σ), whereas we see no emission in the J band. The observed color of SSA22-AzTEC1 in the NIR bands ($J - K > 1.0$) may meet the color criterion ($J - K > 1.4$ in AB) for DRGs (Franx et al. 2003; van Dokkum et al. 2003), which are often found in the universe at $z \sim 2$ and thought to be one of the most massive populations at this epoch (e.g., Kajisawa et al. 2006). This extremely red spectrum in the NIR–MIR strongly suggests that SSA22-AzTEC1 can have a large obscuring column in front of the stellar component and/or an AGN.

We find no significant emission in the Subaru optical B, V, R, i', z', and NB497 images. The photometric data from the Subaru observations are tabulated in Table 1. The non-detection in NB497 does not immediately imply that the

SMA counterpart is not at $z \approx 3.1$ since, due to significant extinction, Lyα emission in $\sim$50% of SMGs with a bright optical counterpart would not be strong enough to be detected in narrow-band imaging (e.g., Chapman et al. 2005). In addition, there are no counterparts in *Hubble* optical (*HST*/ACS F814W) and *GALEX* near/far-ultraviolet images (see Figure 3). The properties in the rest-frame optical images are very similar to those of submillimeter sources with secure (sub)millimeter interferometer identifications, GOODS 850-5 (or GN10; Pope et al. 2005; Wang et al. 2007, 2009; Dannerbauer et al. 2008; Daddi et al. 2009b), HDFN850.1 (Hughes et al. 1998; Downes et al. 1999; Dunlop et al. 2004; Cowie et al. 2009), SXDF850.6 (Hatsukade et al. 2010), and SMA-identified AzTEC sources in the COSMOS field (Younger et al. 2007, 2009).

It is worth noting that in the proximity of SSA22-AzTEC1 ($\simeq 10''$), we find a large emission nebula in the Subaru/NB497 image, which is a corroborated candidate for a Lyα blob at redshift $z = 3.1$ (LAB36, Hayashino et al. 2004). In Figure 1, we show a false-color optical (B, NB497, V) image around SSA22-AzTEC1. Hayashino et al. (2004) have found 74 Lyα blobs over their surveyed area in SSA22 (699 arcmin^2), 59 of which are concentrated in the so-called high-density region (302 arcmin^2) of SSA22, in which SSA22-AzTEC1 is located. The probability that an object has a chance to be closely ($\leqslant 10''$) associated with one of the 59 Lyα blobs over a 302 arcmin^2 region is 1.7%. The separation angle of $\simeq 10''$ corresponds to a projected separation of $\simeq 80h_{70}^{-1}$ kpc in proper scale at $z = 3.1$.

We find a significant X-ray counterpart ($\approx$20 counts), which is listed as source 120 in the Main Source Catalog of the *Chandra* Protocluster Survey, coincident with the SMA source position, suggesting the existence of an accreting massive black hole buried in the dust clouds. The position of the X-ray source is R.A. (J2000) = 22^{h}17^{m}32^s.42 and decl. (J2000) = +0°17′43″.9, and its associated positional error is 0″.54, which is estimated from the 80% confidence interval. The X-ray counterpart has a hard X-ray spectrum (the band ratio[18], BR = $5.53^{+2.93}_{-2.29}$, or the effective photon index[19], $\Gamma_{\rm eff} = -0.34^{+0.57}_{-0.61}$) and is quite bright in the 2–8 keV band (but faint in the 0.5–2 keV band; see also Table 1). In fact the X-ray spectrum is harder than that found for an AGN in a typical SMG among a sample of X-ray luminous SMGs at $z = 0.6$–2.9 (Alexander et al. 2003, 2005a), suggesting that it hosts one of the most heavily obscured distant AGNs known. We will further investigate the X-ray properties in Section 3.6.

3.4. Photometric Redshift Estimates

The important next step is to estimate the redshift of SSA22-AzTEC1. It is extremely difficult to estimate its redshift through conventional optical or NIR spectroscopy because of the faintness in the optical and NIR. Here, we estimate the photometric redshift (photo-z) by fitting the photometric data points to SED templates from stellar population synthesis models (Section 3.4.1) and libraries that simulate MIR-to-radio emission from warm and cold interstellar medium (Section 3.4.2).

3.4.1. Photometric Redshift from NIR Data

We use synthetic SED models of the composite stellar populations (CSPs) with exponentially declining star formation activities from the Bruzual & Charlot (2003) library. We use

---

[18] Ratio of the count rates in the 2.0–8.0 and 0.5–2.0 keV bands.
[19] A parameter for a power-law spectrum defined such that $f \propto \nu^{-\Gamma_{\rm eff}}$, where f and ν are flux and frequency, respectively.

the models to fit the IRAC and MOIRCS photometry as well as the 2σ upper limits in i' and z' bands listed in Table 1, and compute the reduced-χ^2 (i.e., χ^2 dof^{-1}, where dof is the degree of freedom) as a function of redshift:

$$\chi^2 = \frac{1}{N-p} \sum_i \frac{\left(S_{\nu,i}^{\rm obs} - S_{\nu}^{\rm model}\right)^2}{\sigma_i^2}, \qquad (1)$$

where N is the number of photometric data points, p is the number of free parameters, $S_{\nu,i}^{\rm obs}$ and $S_{\nu}^{\rm model}$ are the flux densities from observation and templates, respectively, and σ_i is the uncertainty associated with each photometric datum. Note that we do not use the photometry data at wavelengths $\lambda_{\rm obs} > 3(1+z)\,\mu$m since emission from non-stellar components, such as hot dust, may contaminate the flux densities at $\lambda_{\rm rest} > 3\,\mu$m. We assume the Salpeter (1955) initial mass function and the solar metallicity ($Z = 1\,Z_\odot$). We treat redshift, stellar mass, age, star formation timescale[20], and extinction as free parameters. We make use of the Calzetti et al. (2000) extinction law to account for the extinction with color excess of $E(B-V) =$ 0.0–3.0, which corresponds to visual extinction of $A_V \approx 0$–12. We consider the redshift range from $z = 0$ to 7.

The photo-z derived from fitting the stellar SED of SSA22-AzTEC1 is poorly constrained. We found a minimum of reduced-χ^2 of 0.3 at $z_{\rm phot} \simeq 3.9$ with the confidence interval of $z \geqslant 1.0$ (99% confidence level) or $z \geqslant 2.8$ (68% confidence level). This means that the stellar population synthesis models at any redshift $z \geqslant 2.8$ can easily reproduce the MOIRCS and IRAC SED of SSA22-AzTEC1 and we virtually cannot place strong constraints on the photometric redshift from fitting the MOIRCS and IRAC data to the stellar models.

The primary reason for the poor constraint is that SSA22-AzTEC1 has no notable features in the rest-frame ultraviolet-to-NIR, such as the Lyman break, Balmer break, or the $1.6\,\mu$m stellar bump, which play critical roles in the ultraviolet-to-NIR photometric redshift estimates. As mentioned in the previous section, SSA22-AzTEC1 has an extremely red color in the rest-frame ultraviolet-to-NIR, suggesting a large extinction that makes a steeply declining SED toward shorter wavelengths. Such a steeply declining SED could cause errors in photometric redshift.

An example of such an error can be found in a series of papers on an SMG, GOODS 850-5 (or GN10). Wang et al. (2007, 2009) have reported extremely faint SED of this object over the rest-frame ultraviolet-to-NIR bands (an extremely deep limit to K_S (AB, 2σ) <27.2 mag or 46 nJy). They also found that the photo-z estimates for the ultraviolet-to-NIR data show $z_{\rm phot} \sim 6.5$, whereas the photo-z from its FIR-to-radio ($24\,\mu$m–20 cm) SED shows $z_{\rm phot} \sim 4$. Eventually, Daddi et al. (2009a) blindly searched for CO in this object and found the spectroscopic redshift of $z_{\rm CO} = 4.042$, which as a result rejected the photo-z estimated from the rest-frame ultraviolet-to-NIR.

3.4.2. Photometric Redshift from MIR to Radio Data

Another way to constrain the redshift is to use the FIR-to-radio SED. The ratio between MIR-to-(sub)millimeter and radio flux densities depends on the redshift. This is because in the local universe the radio luminosity is tightly correlated with the FIR luminosity (FIR-to-radio correlation; Helou et al. 1985; Condon

1992; Helou & Bicay 1993; Yun et al. 2001) and this relation seems to hold at high redshifts (e.g., Garrett 2002; Appleton et al. 2004; Ibar et al. 2008; Seymour et al. 2009; Ivison et al. 2010a, 2010b). There have been a number of studies exploiting this relation to constrain the photometric redshift of SMGs (e.g., Carilli & Yun 1999, 2000; Hughes et al. 2002; Aretxaga et al. 2003, 2005, 2007; Wang et al. 2009; Daddi et al. 2009b), and this method can be efficient when a galaxy suffers from extremely heavy extinction in the rest-optical/NIR bands.

We use the available photometry at 24, 860, 1100 μm, and 20 cm data, and employ the SED library from Michałowski et al. (2010) to estimate the redshift of SSA22-AzTEC1. The library consists of SED models, which were developed using the GRASIL code (Silva et al. 1998), that were being fit to the photometric data points (e.g., Hainline et al. 2009) of 76 SMGs with spectroscopic redshifts (Chapman et al. 2005). The mean FIR luminosity, stellar mass, and redshift, averaged over the 76 SMGs, are $L_{\rm FIR} = 10^{12.7}\,L_\odot$, $M_{\rm star} = 10^{11.7}\,M_\odot$, and $z = 2.0$, respectively. To eliminate poorly constrained SEDs from the library, we chose SEDs with robust 24 μm photometry (i.e., SEDs that are well constrained at MIR wavelengths and the Wien tail of the FIR dust emission). We do not use the SEDs that strongly underpredict flux densities at MIR or submillimeter wavelengths ($\lambda_{\rm obs} = 3.6$–8.0, 850 μm). For our final SED templates, we employ 35 SEDs and an averaged SED that is computed by averaging the 35 SEDs. The mean FIR luminosity, stellar mass, and redshift of the 35 SMGs are $L_{\rm FIR} = 10^{12.8}\,L_\odot$, $M_{\rm star} = 10^{11.6}\,M_\odot$, and $z = 2.0$, respectively, which are consistent with those averaged over the 76 spectroscopically identified SMGs. Following Equation (1), we calculate the χ^2 values between the photometric data of SSA22-AzTEC1 and each SED model with varying redshift and luminosity as free parameters. The χ^2 fit to the data at the observed wavelengths of $\lambda_{\rm obs} \geqslant 24\,\mu$m provides a good fit, but the χ^2 fit is poor when we include the $\lambda_{\rm obs} \leqslant 8\,\mu$m data. The $\lambda_{\rm obs} \leqslant 8\,\mu$m data likely suffer from heavy extinction by dust if the data at $\lambda_{\rm obs} \leqslant 8\,\mu$m represent the stellar component of SSA22-AzTEC1. Furthermore, the SED models are biased against an optically faint population of SMGs as noted by Michałowski et al. (2010). Therefore, we use the photometric data at $\lambda_{\rm obs} \geqslant 24\,\mu$m hereafter.

Figure 5(a) (top) shows the reduced χ^2 values for the 35 SED models with 24 μm data (thin curves) and a model averaged over the 35 SEDs (a thick curve), as a function of redshift. Figure 5(a) (bottom) shows the best-fit FIR luminosity that gives the least χ^2 value at each redshift. The χ^2 of the bulk of the SEDs have their local minima at $z \approx 3$. The χ^2 minima, however, scatter broadly in redshift space probably because we have only two dof and many of the SEDs presented in Michałowski et al. (2010) remain poorly constrained especially in the MIR band.

AGN-dominant galaxies could have high dust temperatures, which increases the MIR luminosities and shifts the FIR peak of SEDs to shorter wavelengths. Thus, redshift estimates using such SEDs may tend to be biased toward higher-z. In fact, there are just three SED templates[21] having their local minima at $z \approx 3.8$. Independent measurements of their spectra at rest-frame ultraviolet-to-MIR wavelengths (Swinbank et al. 2004; Takata et al. 2006; Menéndez-Delmestre et al. 2007, 2009; Pope et al. 2008; Hainline et al. 2009) have suggested that they are probably AGN dominant (i.e., AGN is responsible for

---

[20] CSPs are modeled assuming exponentially declined star formation activities. The star formation timescale is defined as e-folding timescale of the star formation activities.

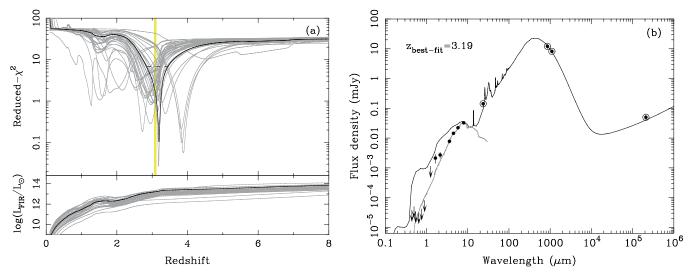[21] SMM J105238.30+572435.8, SMM J123600.15+621047.2, SMM J163650.43+405734.5

Figure 5. Radio-to-MIR photometric redshift of SSA22-AzTEC1. (a) The top panel shows the reduced-χ^2 vs. redshift. Template SEDs are from Michałowski et al. (2010). The gray curves show the reduced-χ^2 for 35 SEDs fit to 24 μm detected SMGs with spectroscopic redshift. The thick solid curve shows that for an SED averaged over the 35 SEDs, and the horizontal dashed line shows the 99% confidence interval. The yellow bar represents the redshift range of the protocluster (z = 3.06–3.12). The bulk of the curves have their local minima at the protocluster redshift, and hence we adopt $z = 3.1$ in the rest of the analyses. The bottom panel shows the infrared luminosities that allow the minimum χ^2 value at each redshift. The details are described in Section 3.4.2. (b) The observed flux densities (filled circles) and the SED (curve, Michałowski et al. 2010) averaged over 35 SMGs with spectroscopic redshift (Chapman et al. 2005). The SED is shifted at the best-fit redshift ($z = 3.19$) and is scaled to the best-fit FIR luminosity (log $L_{\rm FIR}$ = 13.3). Only the data at $\lambda_{\rm obs} \geqslant 24\,\mu$m are used in the χ^2-fit (open circles). The thin curve indicates the best-fit SED model (Maraston 2005) for the stellar component of SSA22-AzTEC1. The rapid dimming and break at $\lambda_{\rm obs} \leqslant 8\,\mu$m is likely due to obscured stellar (and possibly AGN) emission that suffers from extremely heavy attenuation ($A_V \approx 3.4$) of gas and dust in SSA22-AzTEC1. See the text (Section 3.5) for more details.
(A color version of this figure is available in the online journal.)

$\gtrsim$50% of the bolometric luminosity of its host). The AGN of SSA22-AzTEC1 does not appear to dominate the host bolometric luminosity as discussed in the following section (Section 3.6), suggesting that the fits to the AGN-dominated SEDs might not be appropriate. On the contrary, SED templates with lower dust temperature can decrease the best-fit redshift. In our SED fits, local minima are evident at $z \sim 1.5$. The 9.7 μm silicate absorption feature falls to the 24 μm data point at $z \simeq 1.5$, slightly improving the χ^2 fit for this particular redshift. However, the χ^2 values at local minima around low redshifts $z \sim 1.5$ are much larger than those for SEDs with best-fit redshift of $z \sim 3$–4, and the stellar SED fits do not favor redshifts $z \sim 1$. This suggests that the redshift of $z \sim 1.5$ is unlikely.

It is thus reasonable to focus on the averaged SED. The photometric redshift from the averaged SED is $z_{\rm phot} = 3.19^{+0.26}_{-0.35}$ (the error bar is estimated from the 99% confidence interval), consistent with the redshift of the protocluster ($z = 3.06$–3.12). The derived FIR luminosity is $L_{\rm FIR} = 1.9^{+0.4}_{-0.6} \times 10^{13}\,L_{\odot}$ (the error bar is estimated from the 99% confidence interval). The large FIR luminosity implies a star formation rate of $\sim 4 \times 10^3\,M_{\odot}\,{\rm yr}^{-1}$ based on Kennicutt (1998). The best-fit averaged SED along with the photometric data points is shown in Figure 5(b). We note that if we take the best-fit SED model (SMM J123711.98+621325.7) that has the least minimum χ^2 among all of the SEDs, the inferred photometric redshift is $z = 3.18^{+0.26}_{-0.41}$, again consistent with the protocluster redshift. We will hence assume $z = 3.1$ for the redshift of SSA22-AzTEC1 in the rest of the analyses.

3.5. NIR-to-MIR Spectral Energy Distribution

While the Michałowski et al. (2010) SED model is in good agreement with the data at observed wavelengths of $\lambda_{\rm obs} \gtrsim 24\,\mu$m, we see a significant dimming/break in the SED at $\lambda_{\rm obs} \lesssim 8\,\mu$m compared with the SED model. This is probably because of (1) extremely heavy dust extinction of the stellar component, (2) low-mass stellar component, and/or (3) a steep power-law spectrum in rest-frame NIR bands due to hot dust heated by a buried AGN.

To further investigate the possibilities (1) and (2) shown above, we use stellar population SED models to fit the MOIRCS and IRAC photometric data. The method used here is the same as introduced in Section 3.4.1, but we use population synthesis models from the Maraston (2005) and Bruzual & Charlot (2003) libraries and fix the redshift to $z = 3.1$.

The best-fit SED models from Maraston (2005) and Bruzual & Charlot (2003) are essentially consistent, and each of the best-fit SED suggests $A_V = 3.4 \pm 0.2$ mag, an age of $2.5^{+3.0}_{-1.0} \times 10^7$ yr, and a stellar mass of $M_{\rm star} = 7.3^{+7}_{-1.7} \times 10^{10}\,M_{\odot}$ ($\chi^2 = 0.963$, from the Maraston model) and $A_V = 3.4^{+0.4}_{-0.3}$ mag, an age of $2.5^{+5.6}_{-0.9} \times 10^7$ yr, and $M_{\rm star} = 8.2^{+9}_{-1.5} \times 10^{10}\,M_{\odot}$ ($\chi^2 = 0.886$, from the Bruzual & Charlot model). The uncertainties represent the 1σ confidence interval. We model CSPs with e-folding timescale of star formation activities ranging $\tau_{\rm SF} = 0.1$–20 Gyr, but we cannot place a good restriction on the timescale $\tau_{\rm SF}$ because the best-fit SED model is fairly young compared to $\tau_{\rm SF}$. We note that the ages from the stellar model fits are known to be somewhat unreliable, especially for stellar populations in the early universe (Shapley et al. 2005). The extinction is comparable to but slightly larger than those found in SMGs with rest-frame optical spectra obtained by Swinbank et al. (2004, $A_V = 3.0 \pm 1.0$), Borys et al. (2005, $A_V = 1.7 \pm 0.2$), Takata et al. (2006, $A_V = 2.9 \pm 0.5$), and Michałowski et al. (2010, median $A_V = 2.03 \pm 0.95$). Borys et al. (2005) have studied stellar components of 13 SMGs found in the GOODS-N field, and found the stellar masses of $\sim 10^{11}$–$10^{12}\,M_{\odot}$ and a mean stellar mass of $\sim 2 \times 10^{11}\,M_{\odot}$. The stellar mass of

SSA22-AzTEC1 is slightly smaller than those for a typical SMG in GOODS-N. But it is larger than that of coeval ultraviolet-selected star-forming galaxies reported by Shapley et al. (2005, $\log M_{\rm star}/M_\odot = 10.32 \pm 0.51$ for $z \sim 2$) and Magdis et al. (2010, $\log M_{\rm star}/M_\odot = 10.62 \pm 0.11$ for $z \sim 3$), suggesting that SSA22-AzTEC1 is more massive than a coeval typical star-forming galaxy. The SED fit improves ($\chi^2 = 0.106$) if we employ a super-solar metallicity $Z = 2.5\,Z_\odot$ although the best-fit parameters do not change drastically ($A_V = 2.4^{+0.5}_{-0.3}$, an age of $1.6^{+8.4}_{-0.6} \times 10^7$ yr, and $M_{\rm star} = 3.3^{+8}_{-0.5} \times 10^{10}\,M_\odot$). Such higher metallicities are often favored in modeling SEDs of local ultra-luminous infrared galaxies (e.g., Farrah et al. 2005). We note, however, that since the number of the photometric data points at $\leqslant 8\,\mu$m is limited to just six, the parameters (i.e., A_V, age, and $M_{\rm star}$) that determine the stellar SED are highly degenerate and could have large systematic uncertainties.

3.6. Luminous AGN Buried Deeply in SSA22-AzTEC1

Here, we investigate the detailed properties of the X-ray counterpart referred in Section 3.3. We utilize the PIMMS package[22] to model the X-ray spectrum that accounts for the small effective photon index of $\Gamma_{\rm eff} = -0.34^{+0.57}_{-0.61}$. We simulate the intrinsic power-law spectra with photon indices $\Gamma = 1.4$–2.0 behind hydrogen columns in the range $N_{\rm H} = 1 \times 10^{23}$–$4 \times 10^{24}$ cm^{-2}. The spectra are redshifted to $z = 3.1$ and adjusted for absorption through the Galactic hydrogen column toward SSA22-AzTEC1 (4.1×10^{20} cm^{-2}, Kalberla et al. 2005). Other components such as reflection and scattering are not considered. The band ratios between the soft (0.5–2 keV) and hard (2–8 keV) bands, BR, are estimated using PIMMS (v. 3.7a) appropriate for the *Chandra*/ACIS-I Cycle 8 observations. For BR > 3, band ratios do not substantially depend on intrinsic photon index, but depend largely on hydrogen column density. If the AGN has intrinsically a power-law spectrum with a photon index of $\Gamma = 1.8$, which is a typical value for nearby AGNs (Tozzi et al. 2006), the hard spectrum of SSA22-AzTEC1 strongly suggests that the hydrogen column has $N_{\rm H} \sim 1 \times 10^{24}$ cm^{-2} and is almost Compton thick. It should be noted that the band ratio works well for AGNs with $N_{\rm H} \lesssim 5 \times 10^{23}$ cm^{-2} in determining the hydrogen column density, but it becomes less reliable for higher column densities because other components such as reflection and scattering make the X-ray spectrum more complex than just an absorbed power law. However, the X-ray spectral slope is as flat as the heavily obscured SMGs reported by Alexander et al. (2005a) which also appear to have $N_{\rm H} \sim 10^{24}$ cm^{-2}, based on more complex X-ray spectral fitting.

Assuming that the X-ray source is associated with SSA22-AzTEC1 and it is located at $z = 3.1$, the absorption-corrected luminosity in the rest frame 0.5–8 keV, $L_{\rm X}$, is estimated following the expression

$$L_{\rm X} = 4\pi d_{\rm L}^2 F_{\rm X}^{\rm obs}(1 + z)^{\Gamma - 2}, \qquad (2)$$

where $d_{\rm L} = 26.4$ Gpc is the luminosity distance at $z = 3.1$ and $F_{\rm X}^{\rm obs}$ is the absorption-corrected flux in the observed-frame 0.5–8 keV. We find $L_{\rm X} \approx 3 \times 10^{44}$ erg s^{-1}, which is slightly larger than those found in $z \sim 2$ AGN-classified SMGs ($L_{\rm X} \sim 10^{44}$ erg s^{-1}, see Figure 8 of Alexander et al. 2005a). It is therefore likely that SSA22-AzTEC1 hosts a heavily obscured

AGN, which is one of the most luminous objects found among the SMG population.

Given the large X-ray luminosity, the bolometric output from the central AGN in SSA22-AzTEC1 can heat up the interstellar dust and it may contribute to a substantial fraction of the FIR luminosity of the host galaxy. It is becoming clear that AGNs are likely present in a significant fraction of SMGs but their contribution to the FIR emission is in many cases minor (e.g., Alexander et al. 2005a; Menéndez-Delmestre et al. 2009; Hainline et al. 2009; Michałowski et al. 2010). Nevertheless, it is important to investigate the origin of the FIR luminosity of SSA22-AzTEC1 (and hence the intrinsic bolometric output from the AGN) because the AGN-to-host luminosity ratio can be used as an indicator of AGN activity and may provide a hint to the evolutionary phase of the central massive black hole. We now explore what powers the bolometric luminosity of SSA22-AzTEC1–massive star formation or an AGN.

The unabsorbed X-ray to FIR luminosity ratio of SSA22-AzTEC1 is $L_{\rm X}/L_{\rm FIR} = 0.004$. This value is very similar to that found by Alexander et al. (2005a) (median $L_{\rm X}/L_{\rm FIR} \approx 0.004$), but it is an order of magnitude smaller than those found in quasars ($L_{\rm X}/L_{\rm FIR} \approx 0.05$; Elvis et al. 1994; Alexander et al. 2005a). The reason why the luminosity ratio in SSA22-AzTEC1 is so much smaller than those in quasars is the extreme FIR luminosity of SSA22-AzTEC1. In order to estimate the bolometric luminosity of the AGN, we introduce the bolometric correction, which is defined as $f_{\rm bol} \equiv L_{\rm bol}^{\rm AGN}/L_{\rm X}$, where $L_{\rm bol}^{\rm AGN}$ is the bolometric luminosity of the AGN. The bolometric correction for the X-ray band is known to be ~ 10–100 (e.g., Elvis et al. 1994) and to have a moderate dependence on the bolometric AGN luminosity. Marconi et al. (2004) have investigated AGNs in the local universe, and found an empirical relation between $L_{\rm bol}^{\rm AGN}$ and $f_{\rm bol}$ in 2–10 keV band as

$$\log f_{\rm bol} = 1.54 + 0.24\mathcal{L} + 0.012\mathcal{L}^2 - 0.0015\mathcal{L}^3, \qquad (3)$$

where $\mathcal{L}$ is a bolometric luminosity measured in units of $10^{12}\,L_\odot$ and is defined as $\mathcal{L} \equiv \log L_{\rm bol}^{\rm AGN} - 12 = \log f_{\rm bol} + \log L_{\rm X}^{2-10\,{\rm keV}} - 12$. We correct the SSA22-AzTEC1's 0.5–8 keV luminosity to 2–10 keV, and obtain $L_{\rm X}^{2-10\,{\rm keV}} = 10^{10.7}\,L_\odot$ assuming $\Gamma = 1.8$. We solve Equation (3) in terms of $\mathcal{L}$ by substituting $\log f_{\rm bol} = \mathcal{L} - \log L_{\rm X}^{2-10\,{\rm keV}} + 12 = \mathcal{L} + 1.3$ and find $\mathcal{L} = 0.33$. We then have $L_{\rm bol}^{\rm AGN} \approx 10^{12.3}\,L_\odot$ and $f_{\rm bol} \sim 40$ for the AGN of SSA22-AzTEC1. The bolometric correction is consistent with those measured for high-z AGNs ($f_{\rm bol}^{2-10\,{\rm keV}} \approx 35$; Elvis et al. 1994).

This unabsorbed bolometric luminosity of the AGN is extremely large, and as luminous as the most luminous objects in the local universe (e.g., Mrk 231, Soifer et al. 1987). Nonetheless, the bolometric AGN luminosity can only account for $\sim 10\%$ of the huge bolometric output of SSA22-AzTEC1 ($L_{\rm FIR} \approx 2 \times 10^{13}\,L_\odot$). If we adopt the highest estimate for a bolometric correction of the X-ray luminous SMGs ($f_{\rm bol}^{2-10\,{\rm keV}} \approx 70$), the percentage will increase by a factor of ~ 1.6. This suggests that the large FIR luminosity of SSA22-AzTEC1 is not mainly powered by the AGN, but should be attributed to other power sources, likely massive star formation activities.

4. DISCUSSIONS

We have shown that SSA22-AzTEC1 is a hyperluminous starburst galaxy at high redshift, likely $z = 3.1$, and harbors a luminous X-ray source. Here, we discuss a possible scenario for

---

[22] Portable, Interactive Multi-Mission Simulator (PIMMS) is maintained by Koji Mukai, and is available at http://heasarc.nasa.gov/docs/software/tools/.

the growths of the stellar component and massive black hole of SSA22-AzTEC1 in the protocluster environment.

4.1. A Progenitor of a Massive Galaxy in a Protocluster

The inferred redshift and the large stellar mass shown above suggest that we are possibly witnessing the violent forming stage of a massive early-type galaxy that nucleates at the bottom of the gravitational potential underlying *this protocluster*, which can be the archetypical formation site of massive galaxies predicted from the current standard model of structure formation in a CDM universe. There is a claim that the bright end of the evolved systems selected at NIR wavelengths is well populated by $z \sim 2$ but much less in $z \sim 3$ protoclusters around powerful radio galaxies, implying that the bright end of the evolved, likely massive ($\sim 10^{11} M_\odot$) galaxies had first appeared between $z = 2$ and 3 (Kodama et al. 2007). The time duration from $z = 3$ to 2 is ≈ 1.1 Gyr whereas just 0.01 Gyr (i.e., comparable to a lifetime of a massive star) is required for SSA22-AzTEC1 to have $10^{11} M_\odot$ of stars if the stars could be produced at current star formation rate ($\sim 4 \times 10^3 M_\odot$ yr^{-1}) and add another $\sim (2$–$3) \times 10^{10} M_\odot$ to this system. Although we have no information on the mass of the gas reservoir in SSA22-AzTEC1, it is possible for this object to evolve into a $M_{\rm star} \sim 10^{11} M_\odot$ system by $z = 2$. A search for a molecular reservoir in this object will allow us to assess this possibility.

4.2. Growth of a Massive Black Hole in a Protocluster

Comparing the black hole and stellar mass is a good method for understanding the evolutionary status of the AGN in SSA22-AzTEC1. While estimating masses of black holes ($M_{\rm BH}$) is often fairly difficult, there are ways to constrain the black hole mass. One of the most plausible ways using the available data for SSA22-AzTEC1 is to assume the Eddington ratio, η (i.e., ratio of the bolometric to Eddington luminosity of the AGN). When $\eta = 1$, the AGN is powered by Eddington-limited accretion onto the black hole, which virtually provides a lower limit on an estimate of the black hole mass.

Alexander et al. (2008) have investigated $M_{\rm BH}$ and η of spectroscopically identified SMGs in the *Chandra* Deep Field-North. They divided these SMGs into two samples: one is a sample which consists of SMGs that exhibit optical broad emission lines. The other consists of SMGs that host X-ray-identified obscured AGNs with no apparent broad-line region, which is more representative of the overall SMG population than the broad-line SMG sample. The average redshifts of both samples are consistent with the median redshift obtained for radio-identified SMGs ($\langle z \rangle_{\rm median} = 2.2$, Chapman et al. 2005), and their stellar masses are well constrained by Borys et al. (2005). For the broad-line SMGs, one can directly estimate $M_{\rm BH}$ and η using the well-established virial black hole mass estimator (e.g., Wandel et al. 1999; Kaspi et al. 2000). They found the mass ratios $M_{\rm BH}/M_{\rm GAL}$ of the broad-line SMGs and the X-ray-obscured SMGs to be $\sim 2 \times 10^{-3}$ and $\approx 2.9 \times 10^{-4}$, respectively. The average mass ratio of the broad-line SMGs is higher than that of the X-ray-obscured SMGs but lower than those of typical unobscured quasars at $z \sim 2$ ($M_{\rm BH}/M_{\rm GAL} \sim (5$–$10) \times 10^{-3}$, Peng et al. 2006; Coppin et al. 2008). This suggests that the broad-line SMGs have more massive, rapidly growing black holes than the X-ray-obscured SMGs, and they are possibly at a transition phase between X-ray-obscured (i.e., typical) SMGs and unobscured quasars.

Although uncertainties are considerably large, the inferred mass of the black hole in SSA22-AzTEC1 is $M_{\rm BH,Edd} \sim$ $5 \times 10^7 M_\odot$ for Eddington-limited accretion, or $M_{\rm BH} \sim 2.5 \times 10^8 (\eta/0.2)^{-1} M_\odot$. The black hole-to-galaxy mass ratio of SSA22-AzTEC1, which is estimated from the black hole mass divided by the stellar mass, is $M_{\rm BH}/M_{\rm GAL} = 3.5 \times 10^{-3} (\eta/0.2)^{-1}$. The mass ratio is $(1.4$–$3.5) \times 10^{-3}$ if the Eddington ratio has a realistic value between $\eta = 0.2$ and 0.5, which are found to be true in the SMG population (Alexander et al. 2008). This mass ratio is ~ 5–10 times higher than those found for the X-ray-obscured SMGs, but it is below the values found in the $z \sim 2$ unobscured quasars. This large discrepancy might be attributed to the underestimation of the stellar mass, which is difficult to estimate as discussed in Section 3.5. If we underestimate the stellar mass by as large as a factor of 2 (e.g., Shapley et al. 2005), the mass ratio could still be 2.5–5 times larger than those of the X-ray-obscured SMGs. A more likely explanation is that SSA22-AzTEC1 has a more massive black hole accreting at a higher rate (i.e., higher η) than the X-ray-obscured SMGs, but it is less massive than black holes of the quasars. In contrast, the mass ratio is comparable to those of the broad-line SMGs, suggesting that the black hole in SSA22-AzTEC1 can be in the same evolutionary stage as those in the broad-line SMGs. Although the constraints are very uncertain, it is hence possible that the black hole in SSA22-AzTEC1 is being at a transition phase to a quasar, or a *protoquasar* phase (e.g., Sanders et al. 1988; Kawakatu et al. 2003, 2006, 2007; Granato et al. 2004, 2006; Alexander et al. 2005b; Kawakatu & Wada 2009), where the black hole is growing more rapidly than in typical SMGs and is still buried deeply in the central gaseous, dusty "cocoon."

What is the importance of finding a luminous accreting massive black hole, which is one of the most obscured AGNs found in SSA22 and likely resides at the heart of the brightest SMG in the SSA22 protocluster? Large-area submillimeter surveys have suggested that SMGs are related to large-scale structures at high redshift (Blain et al. 2004; Scott et al. 2006; Daddi et al. 2009b, 2009a; Tamura et al. 2009; Viero et al. 2009; Weiß et al. 2009b) even though there is a claim that the population of SMGs cannot always be used as tracers of the most massive dark halos at high-z considering the short time duration (as short as 10 Myr) of their starburst phase (Chapman et al. 2009; Aravena et al. 2010). In particular, Tamura et al. (2009) have found an angular correlation between the positions of the bright SMGs and the Lyα emitters in SSA22, strongly suggesting the physical association of the bright SMGs with the protocluster. In addition, Almaini et al. (2003) have reported strong clustering signals between SMGs and *Chandra* X-ray sources. These observational facts suggest that SMGs which host accreting massive black holes can tightly relate to large-scale structure at high-z, but the evidence for SMGs with heavily obscured AGNs (i.e., protoquasars) forming in high-z protoclusters has not been reported.

Figure 6 shows the position of SSA22-AzTEC1 and the large-scale distributions of luminous objects toward/in the SSA22 protocluster. The high-density region of Lyα emitters in SSA22 consists of at least three large-scale filamentary structures, and the highest density peak (i.e., the apparent protocluster core) actually corresponds to the intersection of these large-scale filaments (Matsuda et al. 2005). SSA22-AzTEC1 is located close to the intersection of the filamentary structures, suggesting that this submillimeter-luminous protoquasar can trace the deepest central potential of the large-scale structure, possibly becoming a powerful AGN, just like high-z radio galaxies and quasars in protoclusters (e.g., McMahon et al. 1994;
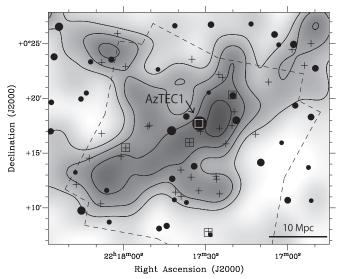
Figure 6. Position of SSA22-AzTEC1 and the large-scale distributions of luminous objects toward/in the SSA22 protocluster; AzTEC sources (filled circles, whose sizes are proportional to 1.1 mm flux densities; Tamura et al. 2009), robust candidates for $z = 3.1$ Lyα blobs (crosses; Matsuda et al. 2004), and the most luminous $z = 3.1$ AGNs in SSA22 with rest 0.5–8 keV luminosities of $L_X \approx (2$–$3) \times 10^{44}$ erg s^{-1} (squares; Lehmer et al. 2009a; Geach et al. 2009). The white square denotes the heavily obscured AGN of SSA22-AzTEC1. The gray scales show the projected number density of Lyα emitters at $z = 3.1$ (Hayashino et al. 2004) and the contours are drawn at (1, 1.5, 2.0, 2.5) times the mean density of the Lyα emitters, which outlines the $z = 3.1$ protocluster. The dashed line shows the field of view of the *Chandra* Deep Protocluster Survey. The bar at bottom-right corner indicates a comoving scale of 10 Mpc at redshift of $z = 3.1$.

Dunlop et al. 1994; Isaak et al. 1994; Ivison 1995; Archibald et al. 2001; Stevens et al. 2003; Reuland et al. 2004; Stevens et al. 2010). Although the accurate redshift of SSA22-AzTEC1 is yet to be determined, this may be the first observational example supporting the long-standing prediction that powerful AGNs preferentially form in high-density environments such as protoclusters (e.g., Sijacki et al. 2007; Colberg & Di Matteo 2008).

Finally, we compare SSA22-AzTEC1 with other objects with AGNs found in SSA22. Within the protocluster, at least over the *Chandra* coverage, no $z = 3.1$ AGNs that exceed SSA22-AzTEC's AGN in X-ray luminosity have been reported. As shown in Figure 6, however, there are three X-ray-identified AGNs at $z = 3.1$ in the innermost part of the protocluster, whose rest-frame 0.5–8 keV luminosities ($L_X \approx (2$–$3) \times 10^{44}$ erg s^{-1}, Lehmer et al. 2009a; Geach et al. 2009) are comparable to that of SSA22-AzTEC1. They have been identified in a Lyα emitter and two Lyα blobs in SSA22.

An $S_{1.1mm} \approx 4$ mJy source (SSA22−AzTEC6, Tamura et al. 2009) could be associated with the X-ray luminous Lyα emitter even though there is no submillimeter interferometric identification. This implies that it might be another example of a protoquasar in the protocluster. However, the effective photon index of the X-ray source ($\Gamma_{eff} = 1.68^{+0.21}_{-0.20}$) is consistent with that of an unobscured AGN, and the host galaxy is clearly visible in the optical broadband images unlike SSA22-AzTEC1. These suggest that gas surrounding the AGN and the stellar component is becoming to clear up. In contrast, the two Lyα blobs within the high-density region are faint at 1.1 mm[23], which does not

---

[23] A SCUBA 3.8σ detection has been reported for one of the Lyα blobs (LAB14, Geach et al. 2005), but we find no significant emission ($S_{1.1mm} < 2$ mJy) in the better-quality AzTEC map.

Table 2
The Properties of SSA22-AzTEC1

Coordinate (J2000)[a]		z_{phot}[b]	L_{FIR}[c]	M_{star}[d]	L_X[e]
R.A.	Decl.		$(10^{13}\,L_\odot)$	$(10^{10}\,M_\odot)$	(erg s^{-1})
$22^h17^m32^s.42$	$+0°17'44''.01$	$3.19^{+0.26}_{-0.35}$	$1.9^{+0.4}_{-0.6}$	$7.3^{+7}_{-1.7}$	$\approx 3 \times 10^{44}$

Notes.
[a] SMA 860 μm position with an uncertainty of $0''.33$.
[b] Photometric redshift estimate. The uncertainty is estimated from the 99% confidence interval.
[c] Far-infrared luminosity. The uncertainty is estimated from the 99% confidence interval.
[d] Stellar mass estimates derived from population synthesis models developed by Maraston (2005). See the text for the details.
[e] The absorption-corrected luminosity in the rest frame 0.5–8 keV.

match the prediction for hosts of protoquasars that vigorous star formation is associated with the early growth of massive black holes. The X-ray sources of the Lyα blobs are unobscured ($\Gamma_{eff} > 1$), which may imply the absence of dense-gas reservoir surrounding the AGNs. Many studies predict that a luminous and unobscured phase of AGN evolution can follow the optically thick phase at which the host is luminous in the FIR and the AGN is buried in dust clouds, as mentioned above (e.g., Kawakatu et al. 2003, 2006). Therefore, we speculate that the AGNs in the Lyα emitter and blobs are possibly at more advanced phase than SSA22-AzTEC1's AGN.

5. CONCLUSIONS AND FUTURE PROSPECTS

Using the SMA, we have identified an 860 μm counterpart to an $S_{1.1mm} = 8.4$ mJy source, SSA22-AzTEC1, which has been previously discovered in a 1.1 mm single-dish survey toward the SSA22 protocluster at $z = 3.1$. We then have investigated intrinsic nature of this source using multiwavelength data all the way from the radio to the X-ray. The derived properties of SSA22-AzTEC1 are summarized in Table 2. Our main findings and conclusions are as follows.

1. We identified an 860 μm counterpart with a flux density of $S_{860\,\mu m} = 12.2 \pm 2.3$ mJy and absolute positional accuracy that is better than $0''.3$. The SMA counterpart is not resolved with the SMA $2''$ beam. The high brightness of this object is not due to strong gravitational lensing by foreground massive objects. (Section 3.1)

2. The SED of SSA22-AzTEC1 is well constrained at wavelengths $\gtrsim 3\,\mu$m, but drops out at a wavelength of $1\,\mu$m ($J > 25.4$ in AB, 2σ, $1''$ aperture) or shorter. This steeply declining spectrum in NIR strongly suggests that SSA22-AzTEC1 can have a large obscuring column in front of the stellar component and/or an AGN. At the SMA position, we see a significant X-ray counterpart (≈ 20 counts), which has a hard X-ray spectrum (the photon index, $\Gamma_{eff} = -0.34^{+0.57}_{-0.61}$; Section 3.3).

3. It is important to determine the redshift of SSA22-AzTEC1 to see if it is located in the protocluster, but a conventional approach using rest-frame optical-to-NIR data does not provide a good constraint on redshift. On the other hand, photometric redshift estimates using MIR (24 μm), submillimeter (860, 1100 μm), and radio (20 cm) data suggest the redshift of SSA22-AzTEC1 to be $z = 3.19^{+0.26}_{-0.35}$, consistent with the protocluster redshift (Section 3.4).

4. We model the NIR-to-MIR SED of SSA22-AzTEC1, and find that the NIR-to-MIR SED requires large extinction

($A_V \approx 3.4$ mag) of starlight from a stellar component with $M_{star} \sim 10^{10.9} M_\odot$ assuming $z \approx 3.1$ (Section 3.5).

5. Modeling of the X-ray spectrum of SSA22-AzTEC1 suggests that it harbors a luminous AGN ($L_X \approx 3 \times 10^{44}$ erg s^{-1}) behind a large hydrogen column ($N_H \approx 1 \times 10^{24}$ cm^{-2}) although it is in general hard to accurately determine L_X and N_H for AGNs with $N_H \lesssim 5 \times 10^{23}$ cm^{-2}. These observed properties of the AGN are very similar to those of the most heavily obscured X-ray luminous SMGs that are likely candidates for *protoquasars*. There are no robust candidates for protoquasars in high-z protoclusters other than SSA22-AzTEC1, and it is thus possible that SSA22-AzTEC1 is the first example of a protoquasar growing at the core of a protocluster (Sections 3.6 and 4.2).

Spectroscopically determining the redshift for SSA22-AzTEC1 is particularly important to confirm the early growth of a massive black hole, as well as its host galaxy, in this high-density environment. Blind searches of CO molecular emission line(s) are necessary for spectroscopically identifying this object that is invisible in the optical and NIR. Zpectrometer (Harris et al. 2007) on the Green Bank Telescope, Z-Spec (Naylor et al. 2003) on Caltech Submillimeter Observatory, EMIR on the IRAM 30 m telescope (e.g., Weiß et al. 2009a), the Redshift Search Receiver (Erickson et al. 2007; Chung et al. 2009) on the Large Millimeter Telescope, the 32 GHz wideband spectrometer on the 45 m telescope at Nobeyama Radio Observatory, and the Atacama Large Millimeter/Submillimeter Array (ALMA, Wootten & Thompson 2009; Iguchi et al. 2009) will perhaps be able to achieve this.

REFERENCES

Alexander, D. M., Bauer, F. E., Chapman, S. C., Smail, I., Blain, A. W., Brandt, W. N., & Ivison, R. J. 2005a, ApJ, 632, 736
Alexander, D. M., Smail, I., Bauer, F. E., Chapman, S. C., Blain, A. W., Brandt, W. N., & Ivison, R. J. 2005b, Nature, 434, 738
Alexander, D. M., et al. 2003, AJ, 125, 383
Alexander, D. M., et al. 2008, AJ, 135, 1968
Almaini, O., et al. 2003, MNRAS, 338, 303
Appleton, P. N., et al. 2004, ApJS, 154, 147
Aravena, M., et al. 2010, ApJ, 708, L36
Archibald, E. N., Dunlop, J. S., Hughes, D. H., Rawlings, S., Eales, S. A., & Ivison, R. J. 2001, MNRAS, 323, 417
Aretxaga, I., Hughes, D. H., Chapin, E. L., Gaztañaga, E., Dunlop, J. S., & Ivison, R. J. 2003, MNRAS, 342, 759
Aretxaga, I., Hughes, D. H., & Dunlop, J. S. 2005, MNRAS, 358, 1240
Aretxaga, I., et al. 2007, MNRAS, 379, 1571
Austermann, J. E., et al. 2009, MNRAS, 393, 1573
Austermann, J. E., et al. 2010, MNRAS, 401, 160
Barger, A. J., Cowie, L. L., Sanders, D. B., Fulton, E., Taniguchi, Y., Sato, Y., Kawara, K., & Okuda, H. 1998, Nature, 394, 248
Bertin, E., & Arnouts, S. 1996, A&AS, 117, 393
Blain, A. W., Chapman, S. C., Smail, I., & Ivison, R. 2004, ApJ, 611, 725
Blain, A. W., & Longair, M. S. 1993, MNRAS, 264, 509
Blain, A. W., Smail, I., Ivison, R. J., Kneib, J.-P., & Frayer, D. T. 2002, Phys. Rep., 369, 111
Borys, C., Scott, D., Chapman, S., Halpern, M., Nandra, K., & Pope, A. 2004, MNRAS, 355, 485
Borys, C., Smail, I., Chapman, S. C., Blain, A. W., Alexander, D. M., & Ivison, R. J. 2005, ApJ, 635, 853
Bruzual, G., & Charlot, S. 2003, MNRAS, 344, 1000
Calzetti, D., Armus, L., Bohlin, R. C., Kinney, A. L., Koornneef, J., & Storchi-Bergmann, T. 2000, ApJ, 533, 682
Carilli, C. L., & Yun, M. S. 1999, ApJ, 513, L13
Carilli, C. L., & Yun, M. S. 2000, ApJ, 530, 618
Chapman, S. C., Blain, A., Ibata, R., Ivison, R. J., Smail, I., & Morrison, G. 2009, ApJ, 691, 560
Chapman, S. C., Blain, A. W., Smail, I., & Ivison, R. J. 2005, ApJ, 622, 772
Chapman, S. C., et al. 2003, ApJ, 585, 57
Chung, A., Narayanan, G., Yun, M. S., Heyer, M., & Erickson, N. R. 2009, AJ, 138, 858
Colberg, J. M., & Di Matteo, T. 2008, MNRAS, 387, 1163
Condon, J. J. 1992, ARA&A, 30, 575
Coppin, K. E. K., et al. 2008, MNRAS, 389, 45
Cowie, L. L., Barger, A. J., Wang, W.-H., & Williams, J. P. 2009, ApJ, 697, L122
Daddi, E., Dannerbauer, H., Krips, M., Walter, F., Dickinson, M., Elbaz, D., & Morrison, G. E. 2009a, ApJ, 695, L176
Daddi, E., et al. 2009b, ApJ, 694, 1517
Dannerbauer, H., Walter, F., & Morrison, G. 2008, ApJ, 673, L127
Di Matteo, T., Springel, V., & Hernquist, L. 2005, Nature, 433, 604
Downes, D., & Solomon, P. M. 2003, ApJ, 582, 37
Downes, D., et al. 1999, A&A, 347, 809
Dunlop, J. S., Hughes, D. H., Rawlings, S., Eales, S. A., & Ward, M. J. 1994, Nature, 370, 347
Dunlop, J. S., et al. 2004, MNRAS, 350, 769
Dye, S., et al. 2008, MNRAS, 386, 1107
Elvis, M., et al. 1994, ApJS, 95, 1
Erickson, N., Narayanan, G., Goeller, R., & Grosslein, R. 2007, in ASP Conf. Ser. 375, From Z-Machines to ALMA: (Sub)Millimeter Spectroscopy of Galaxies, ed. A. J. Baker et al. (San Francisco, CA: ASP), 71
Ezawa, H., Kawabe, R., Kohno, K., & Yamamoto, S. 2004, Proc. SPIE, 5489, 763
Fabian, A. C. 1999, MNRAS, 308, L39
Farrah, D., Surace, J. A., Veilleux, S., Sanders, D. B., & Vacca, W. D. 2005, ApJ, 626, 70
Fazio, G. G., et al. 2004, ApJS, 154, 10
Franx, M., et al. 2003, ApJ, 587, L79
Garrett, M. A. 2002, A&A, 384, L19
Geach, J. E., Smail, I., Chapman, S. C., Alexander, D. M., Blain, A. W., Stott, J. P., & Ivison, R. J. 2007, ApJ, 655, L9
Geach, J. E., et al. 2005, MNRAS, 363, 1398
Geach, J. E., et al. 2009, ApJ, 700, 1
Granato, G. L., De Zotti, G., Silva, L., Bressan, A., & Danese, L. 2004, ApJ, 600, 580
Granato, G. L., Silva, L., Lapi, A., Shankar, F., De Zotti, G., & Danese, L. 2006, MNRAS, 368, L72
Greve, T. R., et al. 2005, MNRAS, 359, 1165
Hainline, L. J., Blain, A. W., Smail, I., Frayer, D. T., Chapman, S. C., Ivison, R. J., & Alexander, D. M. 2009, ApJ, 699, 1610
Harris, A. I., et al. 2007, in ASP Conf. Ser. 375, From Z-Machines to ALMA: (Sub)Millimeter Spectroscopy of Galaxies, ed. A. J. Baker et al. (San Francisco, CA: ASP), 82
Hatsukade, B., et al. 2010, ApJ, 711, 974
Hayashino, T., et al. 2004, AJ, 128, 2073
Helou, G., & Bicay, M. D. 1993, ApJ, 415, 93
Helou, G., Soifer, B. T., & Rowan-Robinson, M. 1985, ApJ, 298, L7
Ho, P. T. P., Moran, J. M., & Lo, K. Y. 2004, ApJ, 616, L1
Hopkins, P. F., Hernquist, L., Cox, T. J., Di Matteo, T., Robertson, B., & Springel, V. 2006, ApJS, 163, 1
Hughes, D. H., et al. 1998, Nature, 394, 241
Hughes, D. H., et al. 2002, MNRAS, 335, 871
Ibar, E., et al. 2008, MNRAS, 386, 953
Ichikawa, T., et al. 2006, Proc. SPIE, 6269, 38
Iguchi, S., et al. 2009, PASJ, 61, 1

Iono, D., et al. 2006a, ApJ, 640, L1
Isaak, K. G., McMahon, R. G., Hills, R. E., & Withington, S. 1994, MNRAS, 269, L28
Ivison, R. J. 1995, MNRAS, 275, L33
Ivison, R. J., Dunlop, J. S., Smail, I., Dey, A., Liu, M. C., & Graham, J. R. 2000, ApJ, 542, 27
Ivison, R. J., Smail, I., Le Borgne, J.-F., Blain, A. W., Kneib, J.-P., Bezecourt, J., Kerr, T. H., & Davies, J. K. 1998, MNRAS, 298, 583
Ivison, R. J., et al. 2010a, MNRAS, 402, 245
Ivison, R. J., et al. 2010b, A&A, 518, L31
Kajisawa, M., et al. 2006, PASJ, 58, 951
Kalberla, P. M. W., Burton, W. B., Hartmann, D., Arnal, E. M., Bajaja, E., Morras, R., & Pöppel, W. G. L. 2005, A&A, 440, 775
Kaspi, S., Smith, P. S., Netzer, H., Maoz, D., Jannuzi, B. T., & Giveon, U. 2000, ApJ, 533, 631
Kauffmann, G. 1996, MNRAS, 281, 487
Kawakatu, N., Anabuki, N., Nagao, T., Umemura, M., & Nakagawa, T. 2006, ApJ, 637, 104
Kawakatu, N., Andreani, P., Granato, G. L., & Danese, L. 2007, ApJ, 663, 924
Kawakatu, N., Umemura, M., & Mori, M. 2003, ApJ, 583, 85
Kawakatu, N., & Wada, K. 2009, ApJ, 706, 676
Kennicutt, R. C., Jr. 1998, ARA&A, 36, 189
Kneib, J.-P., van der Werf, P. P., Kraiberg Knudsen, K., Smail, I., Blain, A., Frayer, D., Barnard, V., & Ivison, R. 2004, MNRAS, 349, 1211
Knudsen, K. K., Kneib, J.-P., Richard, J., Petitpas, G., & Egami, E. 2010, ApJ, 709, 210
Kodama, T., Tanaka, I., Kajisawa, M., Kurk, J., Venemans, B., De Breuck, C., Vernet, J., & Lidman, C. 2007, MNRAS, 377, 1717
Lacy, M., et al. 2004, ApJS, 154, 166
Lehmer, B. D., et al. 2009a, ApJ, 691, 687
Lehmer, B. D., et al. 2009b, MNRAS, 400, 299
Magdis, G. E., Rigopoulou, D., Huang, J.-S., & Fazio, G. G. 2010, MNRAS, 401, 1521
Maraston, C. 2005, MNRAS, 362, 799
Marconi, A., Risaliti, G., Gilli, R., Hunt, L. K., Maiolino, R., & Salvati, M. 2004, MNRAS, 351, 169
Matsuda, Y., et al. 2004, AJ, 128, 569
Matsuda, Y., et al. 2005, ApJ, 634, L125
McMahon, R. G., Omont, A., Bergeron, J., Kreysa, E., & Haslam, C. G. T. 1994, MNRAS, 267, L9
Menéndez-Delmestre, K., et al. 2007, ApJ, 655, L65
Menéndez-Delmestre, K., et al. 2009, ApJ, 699, 667
Michałowski, M., Hjorth, J., & Watson, D. 2010, A&A, 514, A67
Miyazaki, S., et al. 2002, PASJ, 54, 833
Motohara, K., et al. 2005, AJ, 129, 53
Narayanan, D., Hayward, C. C., Cox, T. J., Hernquist, L., Jonsson, P., Younger, J. D., & Groves, B. 2010, MNRAS, 401, 1613
Naylor, B. J., et al. 2003, Proc. SPIE, 4855, 239
Paciga, G., Scott, D., & Chapin, E. L. 2009, MNRAS, 395, 1153
Peng, C. Y., Impey, C. D., Rix, H.-W., Kochanek, C. S., Keeton, C. R., Falco, E. E., Lehár, J., & McLeod, B. A. 2006, ApJ, 649, 616
Perera, T. A., et al. 2008, MNRAS, 391, 1227
Pope, A., Borys, C., Scott, D., Conselice, C., Dickinson, M., & Mobasher, B. 2005, MNRAS, 358, 149
Pope, A., et al. 2008, ApJ, 675, 1171
Reuland, M., Röttgering, H., van Breugel, W., & De Breuck, C. 2004, MNRAS, 353, 377

Rieke, G. H., et al. 2004, ApJS, 154, 25
Salpeter, E. E. 1955, ApJ, 121, 161
Sanders, D. B., Soifer, B. T., Elias, J. H., Madore, B. F., Matthews, K., Neugebauer, G., & Scoville, N. Z. 1988, ApJ, 325, 74
Sault, R. J., Teuben, P. J., & Wright, M. C. H. 1995, in ASP Conf. Ser. 77, Astronomical Data Analysis Software and Systems IV, ed. R. A. Shaw, H. E. Payne, & J. J. E. Hayes (San Francisco, CA: ASP), 433
Scott, S. E., Dunlop, J. S., & Serjeant, S. 2006, MNRAS, 370, 1057
Scott, K. S., et al. 2008, MNRAS, 385, 2225
Scott, K. S., et al. 2010, MNRAS, 405, 2260
Seymour, N., Huynh, M., Dwelly, T., Symeonidis, M., Hopkins, A., McHardy, I. M., Page, M. J., & Rieke, G. 2009, MNRAS, 398, 1573
Shapley, A. E., Steidel, C. C., Erb, D. K., Reddy, N. A., Adelberger, K. L., Pettini, M., Barmby, P., & Huang, J. 2005, ApJ, 626, 698
Sijacki, D., Springel, V., Di Matteo, T., & Hernquist, L. 2007, MNRAS, 380, 877
Silk, J., & Rees, M. J. 1998, A&A, 331, L1
Silva, L., Granato, G. L., Bressan, A., & Danese, L. 1998, ApJ, 509, 103
Smail, I., Ivison, R. J., & Blain, A. W. 1997, ApJ, 490, L5
Smail, I., Ivison, R. J., Blain, A. W., & Kneib, J. P. 1998, ApJ, 507, L21
Soifer, B. T., Sanders, D. B., Madore, B. F., Neugebauer, G., Danielson, G. E., Elias, J. H., Lonsdale, C. J., & Rice, W. L. 1987, ApJ, 320, 238
Solomon, P. M., & Vanden Bout, P. A. 2005, ARA&A, 43, 677
Steidel, C. C., Adelberger, K. L., Dickinson, M., Giavalisco, M., Pettini, M., & Kellogg, M. 1998, ApJ, 492, 428
Steidel, C. C., Adelberger, K. L., Shapley, A. E., Pettini, M., Dickinson, M., & Giavalisco, M. 2000, ApJ, 532, 170
Stevens, J. A., Jarvis, M. J., Coppin, K. E. K., Page, M. J., Greve, T. R., Carrera, F. J., & Ivison, R. J. 2010, MNRAS, 405, 2623
Stevens, J. A., et al. 2003, Nature, 425, 264
Suzuki, R., et al. 2008, PASJ, 60, 1347
Swinbank, A. M., Smail, I., Chapman, S. C., Blain, A. W., Ivison, R. J., & Keel, W. C. 2004, ApJ, 617, 64
Swinbank, A. M., et al. 2010, Nature, 464, 733
Tacconi, L. J., et al. 2006, ApJ, 640, 228
Takata, T., Sekiguchi, K., Smail, I., Chapman, S. C., Geach, J. E., Swinbank, A. M., Blain, A., & Ivison, R. J. 2006, ApJ, 651, 713
Tamura, Y., et al. 2009, Nature, 459, 61
Thompson, A. R., Moran, J. M., & Senson, G. W., Jr. 2001, Interferometry and Synthesis in Radio Astronomy (2nd ed.; New York: Wiley)
Tozzi, P., et al. 2006, A&A, 451, 457
Uchimoto, Y. K., et al. 2008, PASJ, 60, 683
van Dokkum, P. G., et al. 2003, ApJ, 587, L83
Viero, M. P., et al. 2009, ApJ, 707, 1766
Wandel, A., Peterson, B. M., & Malkan, M. A. 1999, ApJ, 526, 579
Wang, W.-H., Barger, A. J., & Cowie, L. L. 2009, ApJ, 690, 319
Wang, W.-H., Cowie, L. L., van Saders, J., Barger, A. J., & Williams, J. P. 2007, ApJ, 670, L89
Weiß, A., Ivison, R. J., Downes, D., Walter, F., Cirasuolo, M., & Menten, K. M. 2009, ApJ, 705, L45
Weiß, A., et al. 2009, ApJ, 707, 1201
Wilson, G. W., et al. 2008a, MNRAS, 386, 807
Wilson, G. W., et al. 2008b, MNRAS, 390, 1061
Wootten, A., & Thompson, A. R. 2009, IEEE Proc., 97, 1463
Younger, J. D., et al. 2007, ApJ, 671, 1531
Younger, J. D., et al. 2009, ApJ, 704, 803
Yun, M. S., Reddy, N. A., & Condon, J. J. 2001, ApJ, 554, 803
Yun, M. S., et al. 2008, MNRAS, 389, 333